

Quantized charge-pumping in higher-order topological insulators

Bing-Lan Wu,^{1,2} Ai-Min Guo,^{3,*} Zhi-Qiang Zhang,^{4,2,†} and Hua Jiang^{4,2}

¹*Gusu Laboratory of Materials, Suzhou 215123, China*

²*Institute for Advanced Study, Soochow University, Suzhou 215006, China*

³*Hunan Key Laboratory for Super-microstructure and Ultrafast Process,*

School of Physics and Electronics, Central South University, Changsha 410083, China

⁴*School of Physical Science and Technology, Soochow University, Suzhou, 215006, China*

(Dated: July 13, 2022)

We study the quantized charge pumping of higher-order topological insulators (HOTIs) with edge-corner correspondences based on the combination of the rotation of in-plane magnetic field and the quantum spin Hall effect. A picture of a specific charge pumping process is uncovered with the help of the non-equilibrium Green's function method. Significantly, we demonstrate that the quantized charge pumping current is achieved without the participation of bulk states, and the charges move along the boundary of the sample. Furthermore, the effects of external parameters on the pumping current is also studied. We find that the magnitude and direction of the pumping current can be manipulated by adjusting the coupling strength between the leads and sample. Our work deepens the understanding of the charge pumping in HOTIs and extends the study of their transport properties.

PACS numbers:

I. INTRODUCTION

As the analog of classical pumping, quantum charge pumping is one of the most important transport phenomena in condensed matter physics [1–21]. The combination of topology and charge pumping has attracted significant interest over the past decades [4–20]. In the study of the quantum Hall [22, 23] and quantum spin Hall effects [24–26], the pumping process can be used to identify the quantization of their topological invariants and suggests the existence of extended edge states in the bulk gap. For the one-dimensional samples, the topological order can always be identified with the help of quantized charge pumping [20, 27]. These studies strongly suggest that the quantized charge pumping is closely related to the intrinsic topological features.

Generally, topological insulators [22–26] exhibit the bulk-boundary correspondence, where the quantized properties can be characterized by bulk states [22]. Therefore, the bulk states always directly participate in the charge pumping process to demonstrate their topological natures. Recently, the concept of higher-order topological insulators (HOTIs) [28–55] has been put forward, which goes beyond the conventional bulk-boundary correspondence. Specifically, the n -th-order HOTI in d -dimension captures the topological states in its $(d - n)$ -dimensional boundaries [28–30] with $n > 1$. For two-dimensional HOTIs, their bulk and edge states are both gapped. However, the zero-energy states locate at the corners of the samples [50–52]. Notably, one of the specific features of HOTIs is that the conventional bulk-

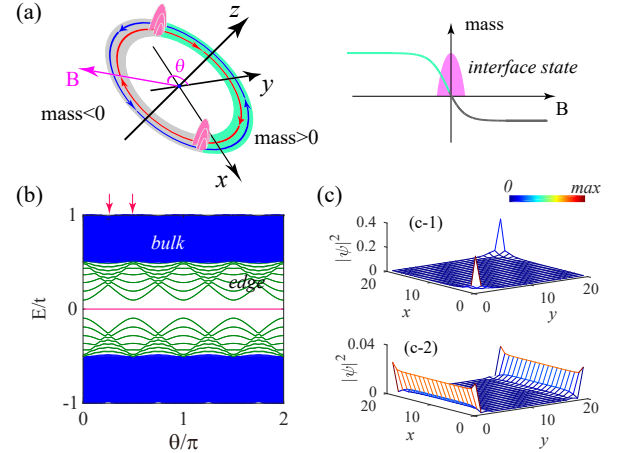


FIG. 1: (a) Schematic diagram of the mass domains for HOTIs. The domain wall ensures the bound states of HOTIs as shown in the right figure. The pink arrows shows the direction of the in-plane magnetic field. (b) The eigenvalues versus angle $\theta = 2\pi f\tau$ with sample size $N \times N = 20 \times 20$. f is the rotational frequency and τ denotes the time. (c) zero-modes' eigenstates for θ marked in (b) with upper: $\theta = \pi/4$; lower: $\theta = \pi/2$.

boundary correspondence could collapse [50], and the corner states characterizing the unconventional topological order of HOTIs could move along the edge of the sample by only manipulating the edge states' mass domain walls [51]. Therefore, a quantized charge pumping without the participation of bulk states may exist. Although the charge pumping in HOTIs has been studied very recently [53, 54], the combination of charge pumping and HOTIs associated with such unique features is rarely reported.

In this work, we propose the charge pumping process

*Electronic address: aimin.guo@csu.edu.cn

†Electronic address: zhangzhiqiangphy@163.com

by manipulating the mass domain walls sitting at the edge of two-dimensional HOTIs [see Fig. 1(a)], which is closely related to the unique features of HOTIs. We uncover that the major characteristic of such a pumping process is that the electrons will be transferred from one corner to its opposite one along the edge instead of through the bulk of the sample. Moreover, the dependence of the external parameters on the pumping current is studied. We find both the magnitude and the direction of the pumping current can be efficiently manipulated. In particular, by adjusting the coupling strength between the leads and sample or the leads' voltages, the current reversal is available.

The rest of this paper is organized as follows: In Sec. II, we present the model and the methods. In Sec. III and Sec. IV, we demonstrate the charge pumping process in HOTIs. In Sec. V, the manipulation of the pumping currents is studied. Finally, a brief discussion and summary are presented in Sec. VI.

II. MODEL AND METHOD

A. model

We consider a modified Bernevig-Hughes-Zhang model with Hamiltonian [51]:

$$H_c = \sum_i \{T_0 c_i^\dagger c_i + [T_x c_{i+\delta_x}^\dagger c_i + T_y c_{i+\delta_y}^\dagger c_i + h.c.]\}, \quad (1)$$

where $T_0 = -B \sin(\theta) \tau_0 \sigma_x + B \cos(\theta) \tau_0 \sigma_y + m \tau_z \sigma_0$ and $T_{x/y} = \frac{t}{2} \tau_z \sigma_0 + \frac{\lambda}{2i} \tau_x \sigma_{x/y}$. $\sigma_{x,y,z}$ ($\tau_{x,y,z}$) are Pauli matrices in spin (orbital) spaces. σ_0 (τ_0) is the 2×2 identity matrix. B is in-plane magnetic field. $\theta = 2\pi f \tau$ denotes the orientation of B varying from 0 to 2π . f is the rotational frequency and τ denotes the time. Parameters are fixed at $m = t$, $\lambda = t$ and $B = 0.5t$ throughout the paper. t is the energy unit with $t = 1$.

Due to the in-plane magnetic field B , mass domain walls sitting at the boundary of the sample appear [51]. As shown in Fig. 1(a), a sample with disk geometry possesses the gapless helical edge states when $B = 0$. After considering the in-plane magnetic field B , the interaction between opposite spins leads to the bandgap for the helical edge states. To be concrete, *mass* terms are introduced into the effective model for the helical edge states. Further, the group velocity of helical edge states changes its sign along the direction of B , which reverses the sign of the mass. The gapped helical edge state with opposite sign of *mass* [*mass* > 0 in the green region and *mass* < 0 in the gray area, see Fig. 1(a)] ensures the existence of the corner states characterizing the topological natures of HOTIs [51].

For simplicity, we consider a square sample, and its eigenvalues versus θ are shown in Fig. 1(b). By checking their zero-energy wavefunction distributions [see Fig. 1(c)], one observes that the corner states emerge in a

certain angle θ . These results indicate that the bound states protected by the mass domain walls rotate with the in-plane magnetic field, as shown in Fig. 1(c). Thus, the charges carried by the bound states rotate by varying θ , which gives rise to the study of charge pumping in HOTIs without the participation of bulk states.

B. method

The charge pumping current is calculated by employing the non-equilibrium Green's function method [56, 57]. Taking a square sample with size $N_x = N_y = N$ as an example, Eq. (1) is rewritten as:

$$H_c = \sum_{n,m=1}^N T_0 c_{n,m}^\dagger c_{n,m} + \sum_{m=1}^N \sum_{n=1}^{N-1} T_x c_{n+1,m}^\dagger c_{n,m} + \sum_{n=1}^N \sum_{m=1}^{N-1} T_y c_{n,m+1}^\dagger c_{n,m} + h.c. \quad (2)$$

Its matrix form \mathcal{H}_c can be written as $H_c = \hat{\mathcal{X}}^\dagger \mathcal{H}_c \hat{\mathcal{X}}$ with the basis $\hat{\mathcal{X}} = [c_{1,1;\alpha}, c_{1,2;\alpha}, \dots, c_{n,m;\alpha}, \dots, c_{N,N;\alpha}]^T$. α stands for the four orbital freedoms of $T_{0/x/y}$. Supposing the eigenequation is $\mathcal{H}_c \psi_j = E_j \psi_j$, one has:

$$\mathcal{H}_c \mathcal{S} = \mathcal{S} \text{diag}[E_1, E_2 \dots E_{4N^2}]. \quad (3)$$

$\mathcal{S} = [\psi_1, \psi_2, \dots, \psi_{4N^2}]$ is constructed by the eigenvectors ψ_j . The coefficient 4 originates from the size of $T_{0/x/y}$. Considering $\hat{\mathcal{X}} = \mathcal{S} \hat{\mathcal{K}}$ with basis $\hat{\mathcal{K}} = [b_1, b_2, \dots, b_{4N^2}]^T$, one has

$$H_c = \hat{\mathcal{X}}^\dagger \mathcal{H}_c \hat{\mathcal{X}} = \hat{\mathcal{K}}^\dagger \mathcal{S}^\dagger \mathcal{H}_c \mathcal{S} \hat{\mathcal{K}} = \sum_{j=1}^{4N^2} E_j b_j^\dagger b_j. \quad (4)$$

Here, E_j is the eigenvalue of the j -th eigenstate. Thus, the following relation is ensured for each basis:

$$c_{n,m;\alpha} = \sum_{j=1}^{4N^2} \psi_j(n, m; \alpha) b_j. \quad (5)$$

$\psi_j(n, m; \alpha)$ is the component of the wavefunction of the j -th eigenvector at site $(n, m; \alpha)$.

The Hamiltonian of the leads and their couplings to the sample can be expressed as [56]:

$$H_{el} = \sum_{\beta,k} \{\varepsilon_{\beta,k} a_{\beta,k}^\dagger a_{\beta,k} + \sum_q t_\beta [a_{\beta,k}^\dagger c_q + h.c.]\}. \quad (6)$$

$q = (1, 1) \equiv \sum_\alpha (1, 1; \alpha)$ and $(N, N) \equiv \sum_\alpha (N, N; \alpha)$ for the left and right leads, respectively. $\beta = L/R$ stands for the left/right lead. After considering Eq. (4), the above equation can be rewritten as:

$$\mathcal{H}_{el} = \sum_{\beta,k} \{\varepsilon_{\beta,k} a_{\beta,k}^\dagger a_{\beta,k} + \sum_{j=1}^{4N^2} t_\beta [\psi_j(o_\beta) a_{\beta,k}^\dagger b_j + h.c.]\}. \quad (7)$$

For simplicity, we set $o_L = (1, 1)$ and $o_R = (N, N)$, which determines the coupling between the left/right lead and the sample's corresponding sites, as shown in Fig. 3(b).

Providing that the occupation number [56] of electron for the j -th energy level is $n_j = \langle b_j^\dagger b_j \rangle$, one has

$$\frac{dn_j}{dt} = \frac{1}{i\hbar} \langle [b_j^\dagger b_j, \mathcal{H}_c + \mathcal{H}_{el}] \rangle. \quad (8)$$

The total occupation number n_j and the components for the leads $n_{j,L/R}$ under the adiabatic approximation satisfy the following forms [57]:

$$\begin{aligned} \frac{dn_j}{d\tau} &= \frac{1}{\hbar} (\tilde{\Gamma}_L f_L + \tilde{\Gamma}_R f_R) - \frac{1}{\hbar} (\tilde{\Gamma}_L + \tilde{\Gamma}_R) n_j, \\ \frac{dn_{j,L/R}}{d\tau} &= \frac{1}{\hbar} \tilde{\Gamma}_{L/R} [f_{L/R}(E_j) - n_j], \end{aligned} \quad (9)$$

where $\tilde{\Gamma}_L = \Gamma_L |\psi_j(1, 1)|^2$ and $\tilde{\Gamma}_R = \Gamma_R |\psi_j(N, N)|^2$. \hbar is the reduced Planck constant. For one-dimensional metallic leads, the related linewidth function can be set as $\Gamma_{L/R} = 2\pi\rho|t_{L/R}|^2$ with the constant ρ the density of states for the leads [56], which represents the coupling between the leads and the sample. Since the similarity transformation \mathcal{S} leads to $\Gamma_{L/R} \rightarrow \tilde{\Gamma}_{L/R}$, the density of states for the sample play key roles, among which $|\psi_j(1, 1)|^2$ and $|\psi_j(N, N)|^2$ are the electron density of the j -th eigenvectors for sites $(n, m) = (1, 1)$ and (N, N) , respectively. $f_{L/R} = [1 + e^{\frac{E_F + V_{L/R}}{k_B T_0}}]^{-1}$ is the Fermi-Dirac distribution function. $V_{L/R}$ is an additional voltage potential on the left/right lead, k_B is the Boltzmann constant. T_0 is the temperature and is fixed to $T_0 \rightarrow 0$.

Generally, the current for the j -th eigenvalue can be represented as

$$I_{j,L/R} = ef \oint dn_{j,L/R}, \quad (10)$$

with $I_{L/R} = \sum_{j=1}^{4N^2} I_{j,L/R}$, which is a function of n_j . The integration is over one period. The occupation number n_j can be obtained by solving Eq. (9) self-consistently in one periodic, and the current is available as well. Importantly, to simulate the high-frequency rotation, which is essential for adiabatic charge pumping, $d\tau = 10^{-6}s$ is adopted hereafter. Supposing $[0, 2\pi]$ is divided into l intervals, one has $f \approx 1/(ld\tau)$. The variation of $d\tau$ does not change the main results of this paper. Due to the existence of band gaps [see Fig. 1(b)], n_j for both bulk and edge states are insensitivity to the rotational angle θ , and the corresponding $I_{j,L/R}$ can be neglected. We next only pay attention to the charge pumping of zero-energy modes, which is closely related to the corner states of the HOTIs.

III. ELIMINATING THE INFLUENCE OF FINITE SIZE EFFECT

Significantly, a constrain in our numerical method should be considered. If ψ_j describes a corner state, such

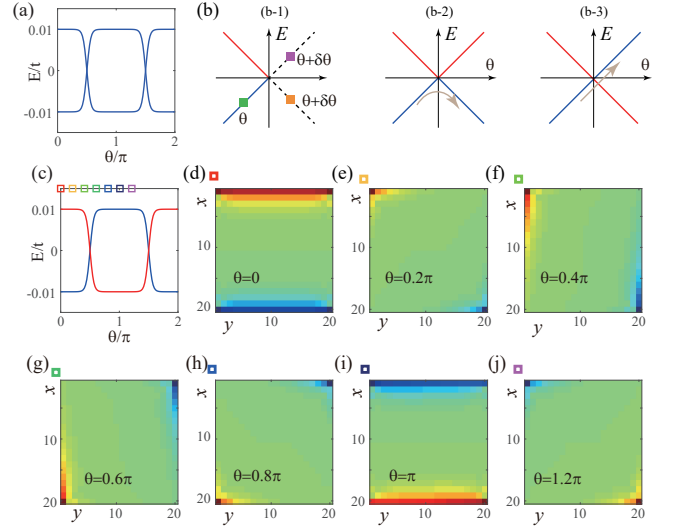


FIG. 2: The voltage potential H_U is introduced to eliminate the degenerate perturbation between two corners due to the finite size effect. H_U satisfies Eq. (11). (a) The evolution of the corner states with $U = 0.01t$. (b-1) shows the degenerate point of eigenvalues in (a). (b-2) and (b-3) are two possible evolution paths by increasing θ . (c) is the obtained evolution path based on the adiabatic features of the pumping process. (d)-(j) are the wavefunctions for the red and blue lines in (c) by varying θ .

a corner state must be isolated. Fortunately, this condition can be easily satisfied in realistic samples. The environment (e.g. disorder, the coupling between the leads, etc.) will induce the energy difference, and their values are much larger than the coupling strength between two corner states. Nevertheless, in order to simulate a faithful charge pumping process, one should eliminate the finite size effect in numerical calculation. Due to the finite size effect, there exists a weak coupling between the zero-energy corner states, which can be dealt with by the degenerate perturbation. Such a degenerate perturbation dramatically changes the definition of the $n_j = \langle b_j^\dagger b_j \rangle$ and significantly influences the charge pumping as follows.

Taking $\theta = 0.25\pi$ as an example, the zero-energy states for different corners can be marked as $|1, 1\rangle$ and $|N, N\rangle$. After considering the coupling strength Δ induced by the finite size effect, the effective perturbation Hamiltonian for these zero-energy modes reads $\begin{bmatrix} 0 & \Delta \\ \Delta & 0 \end{bmatrix}$. For $\Delta = 0$, its eigenfunctions are $|\varphi_1\rangle = |1, 1\rangle = [1, 0]^T$ and $|\varphi_2\rangle = |N, N\rangle = [0, 1]^T$, with eigenvalues $\varepsilon_1 = \varepsilon_2 = 0$. T stands for the transpose. By contrast, for $\Delta \neq 0$ [no matter how weak Δ is], the degenerated zero energy states are lifted by the degenerate perturbation, and the eigenfunctions become $|\varphi_{1,2}\rangle = \frac{1}{\sqrt{2}}[|1, 1\rangle \pm |N, N\rangle]$. Then, a well defined $n_j = \langle b_j^\dagger b_j \rangle$ for each corner state is not available. More importantly, the charge hopping between the sample and the left/right lead will happen non-locally

when $\Delta \neq 0$. Such a nonlocal feature is improper since the transport between the leads and the sample occurs locally in the experiment. As a result, Δ and the degenerate perturbation should be eliminated to simulate the experimental setups.

To overcome such a problem, we introduce an additional perturbation in Eq. (2), where a step-potential along the x direction is adopted [58]:

$$H_U = \sum_{n,m} 2U \left[\frac{1}{2} - \Theta\left(\frac{N}{2} - n\right) \right] \tau_0 \sigma_0 c_{n,m}^\dagger c_{n,m}. \quad (11)$$

U represents the small voltage potential, and $\Theta(N/2 - n)$ is the step function. Figure 2(a) plots the eigenvalues versus θ for the corner states with $U = 0.01t$.

The second question is that the evolution of eigenvalues of the corner states versus θ intersects two times during one pumping cycle after considering Eq. (11) [see Fig. 2(a)]. The evolution paths are ambiguous at the crossing points, where there are two possible cases [see Fig. 2(b)]. Nevertheless, the charge pumping process should preserve the adiabatic features [23] with the eigenfunctions evaluated continuously. Based on the continuity condition of eigenfunctions, one is able to identify the correct evolution path by comparing the overlap of wavefunctions. Specifically, we denote the eigenfunctions for the green, orange and purple dots in Fig. 2(b-1) as $\psi_{\theta,j}$, $\psi_{\theta+\delta\theta,j}$, and $\psi_{\theta+\delta\theta,j+1}$. Since $|\langle\psi_{\theta,j}|\psi_{\theta+\delta\theta,j+1}\rangle|^2 > |\langle\psi_{\theta,j}|\psi_{\theta+\delta\theta,j}\rangle|^2$ for $\delta\theta \rightarrow 0$, the eigenfunctions evolve along the path shown in Fig. 2(b-3).

Now, we capture the reasonable eigenvalue and eigenvector evolutions for different corner states as shown in Figs. 2(d)-(j). The colors of the plots, marked in red and blue, correspond to the red and blue eigenvalues shown in Fig. 2(c), respectively. It is obvious that the wavefunctions for different corners are completely decoupled. Furthermore, the wavefunctions are always localized at the edge or corner rather than the bulk, which is unique for the HOTIs. Based on the above results, we can study the charge pumping in realistic samples.

IV. QUANTIZED CHARGE PUMPING BASED ON THE MASS DOMAIN WALLS OF HOTI

As presented in the previous section, the domain wall-protected boundary states rotate with magnetic field. When a lead is coupled with the sample, the charges carried by the bound states will jump into the lead or vice versa, and the charge pumping current becomes available. In this section, we present the picture of quantized charge pumping based on the corner states of HOTIs. Figure 3(b-1) displays the schematic diagram of the charge pumping setup. The leads' Fermi energy is fixed to $E_F = 0$ with $V_{L/R} = 0$, and the linewidth function is set as $\Gamma_L = \Gamma_R = \Gamma = 10^{-6}t$ [57] unless otherwise noted.

Before proceeding, we have a few remarks based on Eq. (9), which are important to clarify the charge pump-

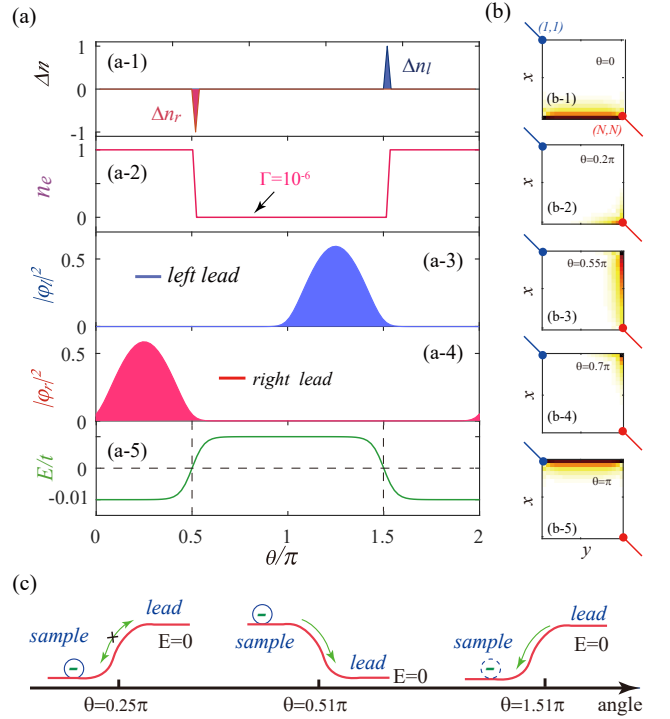


FIG. 3: (a-1) is the evolution of the varied charge density $\Delta n_{r,l}$ versus $\theta = 2\pi f\tau$ for the right lead (red) and left lead (blue), respectively. $f = 10^4$ is adopted without specific statement. (a-2) The evolution of the occupation number n_e versus θ . (a-3) and (a-4) are the eigenstates $|\varphi_l|^2$ and $|\varphi_r|^2$ for the eigenenergy shown in (a-5), respectively. (a-5) is the eigenenergy versus θ . Since the two curves in Fig. 2(e) can be analyzed in a similar manner, we only pay attention to one of the curves. The corresponding wavefunctions for different θ are shown in (b-1)-(b-5). The blue and red marks denote the left and right leads and the contact points. The parameters are $U = 0.01t$, $E_F = 0$ and $\Gamma = 10^{-6}t$. (c) shows three schematic diagrams of charge transfer processes for typical θ in (a). The solid (dashed) circle indicates that the energy level is filled (empty) with $n_e = 1$ ($n_e = 0$). The red solid lines mark the energy for the sample and the lead. From left to right: electron transfer is forbidden; from sample to lead; from lead to sample.

ing process. (i) The pumping current $I_{L/R}$ and the occupation number n_j dramatically depend on $\tilde{\Gamma}_{L/R} = \Gamma_{L/R} |\psi_{l/r}|^2$. Here, $\psi_l = \psi_j(1, 1)$ and $\psi_r = \psi_j(N, N)$. This implies that the corresponding $\tilde{\Gamma}_{L/R}$ is non-zero if $\psi_{l,r} \neq 0$. For $\tilde{\Gamma}_{L/R} \neq 0$, the sample can exchange charges with the leads. (ii) Aside from $\tilde{\Gamma}_{L/R}$, the variation of n_j also relies on the relative values of the eigenvalue $E_{\theta,j}$ for the sample and the Fermi energy E_F for the leads, as shown in Fig. 3(c). When the leads are coupled with the sample's eigenvectors with $\psi_{l/r} \neq 0$, electrons will transfer from the lead to the sample in the case of $E_{\theta,j} < E_F$. Alternatively, electrons will be transferred from the sample to the lead when $E_{\theta,j} > E_F$.

Now, we demonstrate the pumping process by manip-

TABLE I: Several typical charge exchange processes for different θ in Fig. 3(a). E is the energy plotted in Fig. 3(a-5). E_F is the Fermi energy for the leads. The first row shows the θ for the corresponding quantities. For instance, n_e is the occupation number slightly before θ [i.e., $\theta - \delta\theta$].

θ	θ	θ	$\theta - \delta\theta$	events at θ
$\varphi_r \neq 0$	$\varphi_l = 0$	$E < E_F$	$n_e = 1$	no charge exchange
$\varphi_r \neq 0$	$\varphi_l = 0$	$E > E_F$	$n_e = 1$	discharge at right lead
$\varphi_r = 0$	$\varphi_l = 0$	$E > E_F$	$n_e = 0$	no charge exchange
$\varphi_r = 0$	$\varphi_l \neq 0$	$E > E_F$	$n_e = 0$	no charge exchange
$\varphi_r = 0$	$\varphi_l \neq 0$	$E < E_F$	$n_e = 0$	charge at left lead
$\varphi_r = 0$	$\varphi_l = 0$	$E < E_F$	$n_e = 1$	no charge exchange

ulating the bound states of the domain wall-protected HOTIs. For simplicity, we only pay attention to one of the corner states [$j = 2N^2$ for $\theta = 0$] since they are decoupled, and the rest case can be analyzed in a similar manner. We display the evolution of several typical quantities in Figs. 3(a-1)-(a-5). It plots the wavefunctions coupled to the left/right lead $|\varphi_{r/l}|^2 \equiv |\psi_{\theta,j;r/l}|^2$; the corresponding eigenenergy $E \equiv E_{\theta,j}$ and the occupation number $n_e \equiv n_j$. Here, n_j is calculated numerically by solving Eq. (9) self-consistently.

At the beginning of the pumping with $\theta = 0$, states with energy E smaller than E_F are occupied (i.e., $n_e = 1$), and the wavefunction $|\varphi_{r,l}|^2$ is concentrated at the lower boundary [see Figs. 3(b) and (c)]. Although the eigenstates are coupled with the right leads [$\tilde{\Gamma}_R \neq 0$], charge exchange is not available since the state is fully occupied with $n_e = 1$ and $E < E_F$. With the increasing of θ , the corner state localized at (N, N) emerges and correspondingly $|\varphi_r|^2$ reaches its maximum. By further increasing θ , the wavefunction gradually extends along the x direction and moves toward the higher energy. Notably, for the critical $\theta = \pi/2$ where $E = E_F$, the wavefunctions are still coupled to the right lead with $|\varphi_r|^2 \neq 0$ [see Figs. 3(a-3) and (b-3)]. Therefore, the charge will be transferred from the sample to the right lead [see Fig. 3(c)] when $\theta > \pi/2$, which corresponds to the discharging process with $\Delta n_r \equiv dn_{j,R} = -1$. Then, the state is empty, and n_e drops to zero [see Fig. 3(a-2)].

A similar analysis can be applied for the rest half of the cycle, and the charging process is achieved at the left lead. In simple terms, the whole pumping process is to discharge at the right and charge at the left lead, as summarized in TABLE. I. Consequently, one electron is transferred from the left lead to the right one during each cycle. Because of the existence of two equivalent energy levels, the system pumps a total of two electrons, which is quantized in one period. We have to emphasize that the charge is carried by the corner states and do not pass through the bulk during the pumping process, which is unique for HOTIs.

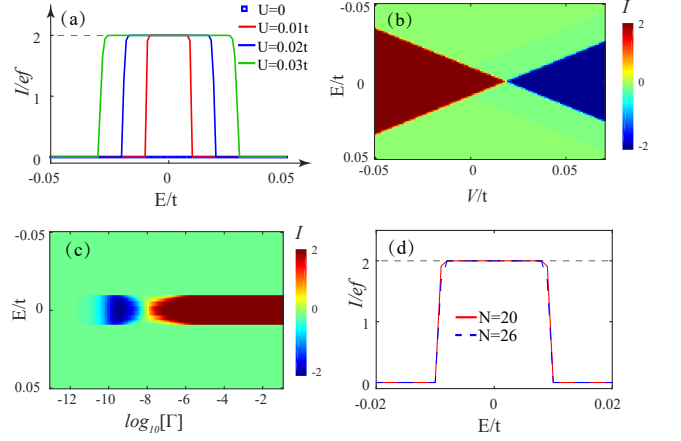


FIG. 4: (a) Pumping current $I = I_L$ versus Fermi energy E for different U . (b) Pumping current I versus (E, V) with $\pm V/2$ the additional voltage potential on left ($-V/2$) and right leads ($V/2$) with $V_{L/R} = \pm V/2$. (c) I versus E and $\log_{10}[\Gamma]$. Γ is the linewidth function for leads, which denotes the coupling strength between the leads and the sample. (d) The sample size dependence of I versus E .

V. MANIPULATING THE PUMPING CURRENT

Having established the pictures of charge pumping process in HOTIs, we investigate the effect of external parameters on the pumping current in this section. Since the conservation of current, i.e., one has $I_L = -I_R$, we only focus on I_L in the following.

As illustrated in Fig. 4(a), the current I_L in the left lead is zero when the voltage potential $U = 0$ because the degenerate perturbation between different corners does not allow the charging and discharging processes to occur independently. As clarified in Sec. III, such a case cannot happen in realistic materials. However, once the voltage potential U is introduced, the charge pumping appears and gives rise to plateaus of quantized currents, even for $U = 0.01$. By further increasing U , the quantized current plateau becomes wider because the energy range of the $E - \theta$ curve broadens, as shown in Fig. 3(a-5). Besides, the current I is almost unchanged by increasing N [see Fig. 4(d)], manifesting that the quantized charge pumping is insensitive to the sample size N .

When the voltage potentials $V_L = -\frac{V}{2}$ and $V_R = +\frac{V}{2}$ for the leads are considered, the effective Fermi energy for the leads are modified to $E_F + V_{L/R}$. As shown in Fig. 4(b), V can adjust the quantized pumped current I and can even reverse the sign of I . Compared with $V = 0$ in Fig. 3(a), V changes the relative energy between the leads and the sample, thus affecting the charging and discharging processes. For $V < 0$, the jump point of n_j shifts to smaller (larger) θ [lower (higher) energy] for the right (left) lead, which maintains the direction of the pumping current. While for $V > 0$, the jump point of

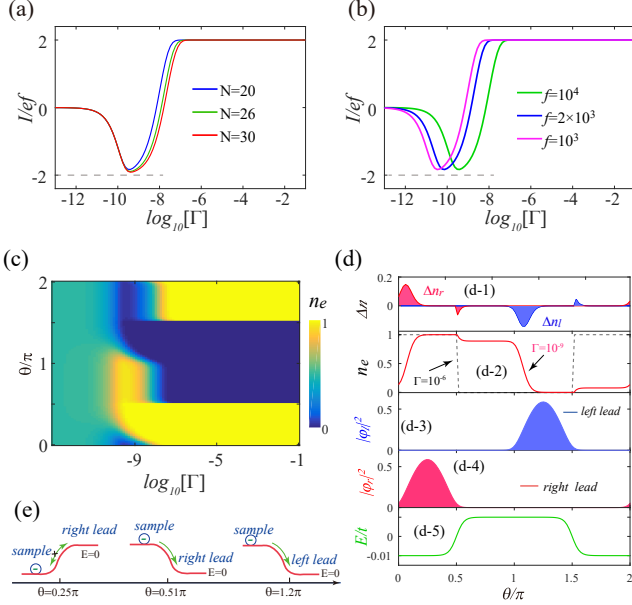


FIG. 5: (a) Pumping current I versus $\log_{10}[\Gamma]$ for different sample size N . (b) I versus $\log_{10}[\Gamma]$ for the frequency f with $\theta = 2\pi f\tau$. (c) Occupation number n_e for eigenvalue $E_{j=2N^2}$ versus angle θ and $\log_{10}[\Gamma]$. (d-1)-(d-5) The n_e , Δn and $|\phi_{l/r}|^2$, E versus θ . The parameters are the same with Fig. 3 except $\Gamma = 10^{-9}t$. (e) shows three schematic diagrams of charge transfer process for different θ in (d).

n_j moves toward larger (smaller) θ for the right (left) lead. When $E_F - |V_L| < |U|$ and $E_F + |V_R| > |U|$, the direction of the pumping current should be reversed since the discharging process in the right lead is unavailable.

Interestingly, similar phenomena can also be observed in Fig. 4(c), where the coupling strength Γ for the leads can also adjust the magnitude and the direction of I . The reversal of I induced by Γ is seldom reported in previous studies and will be analyzed in detail below.

First, we need to rule out the influence of finite size effect and rotational frequency f . Figure 5(a) shows the pumping current I versus $\log_{10}[\Gamma]$ for different sample size N . As N increases, the reversal persists, demonstrating that the reversal is not attributed to the finite size effect. Importantly, since the wavefunctions of the bound states become more localized for a larger sample size, $\tilde{\Gamma}_{L/R} = \Gamma|\psi_{l/r}|^2$ decreases in this case. Thus, the critical point, where I changes its sign, moves towards higher Γ . Similarly, the variation of rotational frequency f does not affect the current reversal either [see Fig. 5(b)]. Nevertheless, the lower the frequent f is, the easier it is for leads to exchange charges with the sample. Namely, decreasing f is equivalent to enhancing Γ , and the critical point shifts toward the lower Γ as f decreases [see Fig. 5(b)].

According to the above results, the reversal of I only depends on the Γ and it is a physically reliable process. We then investigate the occupation number n_e versus

$(\theta, \log_{10}[\Gamma])$. Comparing Figs. 5(a) and (c), it is clear that I deviates from the quantized value when the occupation number n_e versus θ significantly changes. Besides, n_e changes its value as Γ decreases in some regions. The state which is originally occupied [$n_e = 1$] becomes empty [$n_e = 0$], and the empty state is occupied. Accordingly, the current is reversed since the occupation numbers are approximately opposite for large and small Γ .

For the sake of clarity, we plot n_e , Δn and $|\phi_{l/r}|^2$, E in Figs. 5(d-1)-(d-5) in the case of weak coupling $\Gamma = 10^{-9}t$, which accounts for the current reversal. We start from the point with $n_e = 1$ such as $\theta = 0.25\pi$. As θ exceeds 0.5π , the energy of the bound state E surpasses the leads' Fermi energy E_F . Therefore, the occupation number n_e starts to decrease, which seems to be the same as the case of $\Gamma = 10^{-6}t$. Nevertheless, unlike the case with larger Γ [see Fig. 5(d-3)], n_e does not directly reduce from one to zero. The occupation number only changes slightly with $|\Delta n| \ll 1$ [see Figs. 5(d-1) and (d-2)]. Thus, an almost fully filled state preserves when it leaves the right lead although $E > E_F$ is achieved.

Continuing to increase θ , the remaining electrons should be released in the left lead since $E > E_F$ still holds. Because of the sufficiently long discharge time in the left lead, almost all the charges are released in the left lead [see Figs. 5(d-2) and (c)]. Similarly, an almost empty state leaves the left lead with the charging process negligible. Thus, the charge pumping processes in the left and right leads are opposite to those in Fig. 3(a), which induces the reversal of the pumping current. In short, the reversal of the pumping current arises from the insufficient discharge and charge processes in the right and left leads, respectively.

VI. CONCLUSION

In summary, the quantized charge pumping in HOTIs is studied. We found an interesting charge pumping process based on the unique topological natures of the HOTIs, which is distinct from the widely studied ones. The charges only shift along the sample's boundary, and the bulk states do not directly participate in the pumping process. Significantly, the bulk states ensure the existence of gapped edge states, so the high-order topological order is essentially required for the pumping process. Furthermore, the manipulations of the pumping current by external parameters are also uncovered. We find that the direction of the pumping current strongly depends on the coupling strength and the chemical potential of the leads. Our work extends the understanding of exotic transport properties in HOTIs.

VII. ACKNOWLEDGEMENTS

We are grateful to Qiang Wei, Hongfang Liu, Rui-Chun Xiao, Chui-Zhen Chen and especially Qing-feng Sun for

fruitful discussions. This work was supported by the National Basic Research Program of China (Grant No. 2019YFA0308403), NSFC under Grant No. 11822407 and No. 12147126. A.M.G. acknowledges supports from

the NSFC under Grant No. 11874428 and the High Performance Computing Center of Central South University .

-
- [1] B. L. Altshuler, and L. I. Glazman, Pumping electrons. *Science* **283**, 1864 (1999).
 - [2] M. Wagner, and Sols. F, Subsea Electron Transport: Pumping Deep within the Fermi Sea, *Phys. Rev. Lett.* **83**, 21(1999).
 - [3] Z. Yu, and F. Xu, Valley-polarized pumping current in zigzag graphene nanoribbons with different spatial symmetries, *Chin. Phys. B* **27**, 127203 (2018).
 - [4] D. J. Thouless, Quantization of particle transport, *Phys. Rev. B* **27**, 6083 (1983)
 - [5] D. Y. H. Ho and J. Gong, Quantized adiabatic transport in momentum space, *Phys. Rev. Lett.* **109**, 010601 (2012).
 - [6] S. Nakajima, T. Tomita, S. Taie, T. Ichinose, H. Ozawa, and L. Wang, et al., Topological thouless pumping of ultracold fermions, *Nat. Phys.* **12**, 296 (2016).
 - [7] M. Lohse, C. Schweizer, O. Zilberberg, M. Aidelsburger, and I. Bloch, A thouless quantum pump with ultracold bosonic atoms in an optical superlattice. *Nat. Phys.* **12** (2016).
 - [8] M. J. Wang, J. Wang, and J. F. Liu, Quantized spin pump on helical edge states of a topological insulator, *Sci. Rep.* **9**, 3378 (2019).
 - [9] K. Hattori, Topological Pumping of Spin-Polarized Currents through Helical Edge States Due to Dynamically Generated Mass Gap, *J. Phys. Soc. Jpn.*, **82**, 24708 (2013).
 - [10] E. R. Mucciolo, C. Chamon, and C. M. Marcus, Adiabatic quantum pump of spin-polarized current, *Phys. Rev. Lett.* **89**, 146802 (2002)..
 - [11] S. K. Watson, R. M. Potok, C. M. Marcus, and V. Umansky, Experimental Realization of a Quantum Spin Pump, *Phys. Rev. Lett.* **91**, 258301 (2003).
 - [12] W. Zheng, J. Wu, B. Wang, J. Wang, Q. Sun, and H. Guo, Parametric quantum spin pump, *Phys. Rev. B* **68**, 113306 (2003).
 - [13] O. Mosendz, V. Vlaminck, J. E. Pearson, F. Y. Fradin, G. E. W. Bauer, S. D. Bader, and A. Hoffmann, Detection and quantification of inverse spin Hall effect from spin pumping in permalloy/normal metal bilayers, *Phys. Rev. B* **82**, 214403 (2010).
 - [14] F. Mahfouzi, B. K. Nikolic, S. H. Chen, and C. R. Chang, Microwave-driven ferromagnet-topological-insulator heterostructures: the prospect for giant spin battery effect and quantized charge pump devices, *Phys. Rev. B* **82** (2010).
 - [15] J. Wang, and J. F. Liu, Quantized charge pump of massive Dirac electrons, *Phys. Rev. B* **95** 205433 (2017)
 - [16] M. Blaauboer, and C. M. L. Fricot, Spin pump turnstile: Parametric pumping of a spin-polarized current through a nearly closed quantum dot, *Phys. Rev. B* **71**, 41303 (2005).
 - [17] Y. Tserkovnyak, A. Brataas, and G. E. W. Bauer, Spin pumping and magnetization dynamics in metallic multilayers, *Phys. Rev. B* **66**, 224403 (2002).
 - [18] B. Wang, J. Wang, and H. Guo, Parametric pumping at finite frequency, *Phys. Rev. B* **65**(7), 73306 (2002).
 - [19] M. Moskalets, and M. Buttiker, Floquet scattering theory of quantum pumps, *Phys. Rev. B* **66**(20), 205320 (2002).
 - [20] L. Wang, M. Troyer, and X. Dai, Topological Charge Pumping in a One-Dimensional Optical Lattice, *Phys. Rev. Lett.* **111**, 26802 (2013).
 - [21] M. Thakurathi, J. Klinovaja, and D. Loss, From fractional boundary charges to quantized Hall conductance, *Phys. Rev. B* **98**, 245404 (2018); K. Laubscher, C. S. Weber, D. M. Kennes, M. Pletyukhov, H. Schoeller, D. Loss, and J. Klinovaja, Fractional boundary charges with quantized slopes in interacting one- and two-dimensional systems, *Phys. Rev. B* **104**, 035432 (2021).
 - [22] K. V. Klitzing, G. Dorda, and M. Pepper, New method for high-accuracy determination of the fine-structure constant based on quantized Hall resistance, *Phys. Rev. Lett.* **45**, 494 (1980).
 - [23] David Tong, Lectures on the Quantum Hall Effect, arXiv: 1606.06687; R. B. Laughlin, Quantized Hall conductivity in two dimensions, *Physical Review B* **23**, 5632 (1981).
 - [24] M. N. Chen, L. Sheng, R. Shen, D. N. Sheng, and D. Y. Xing, Spin Chern pumping from the bulk of two-dimensional topological insulators, *Phys. Rev. B* **91**, 125117 (2015).
 - [25] M. Z. Hasan, and C. L. Kane, Colloquium: Topological insulators, *Rev. Mod. Phys.* **82** (2010).
 - [26] M. König, S. Wiedmann, C. Brüne, A. Roth, H. Buhmann, L. W. Molenkamp, X. L. Qi, and S. C. Zhang, Quantum spin Hall insulator state in HgTe quantum wells, *Science* **318**, 766 (2007).
 - [27] Ning Sun and Lih-King Lim, Quantum charge pumps with topological phases in a Creutz ladder, *Phys. Rev. B* **96**, 035139 (2017).
 - [28] W. A. Benalcazar, B. A. Bernevig, and T. L. Hughes, Quantized electric multipole insulators, *Science* **357**, 61 (2017).
 - [29] W. A. Benalcazar, B. A. Bernevig, and T. L. Hughes, Electric multipole moments, topological multipole moment pumping, and chiral hinge states in crystalline insulators, *Phys. Rev. B* **96**, 245115 (2017).
 - [30] Q. Wang, D. Wang, and Q. H. Wang, Entanglement in a second-order topological insulator on a square lattice. *EPL*, **124**, 50005 (2018).
 - [31] F. Schindler, A. M. Cook, M. G. Vergniory, Z. Wang, S. S. P. Parkin, B. A. Bernevig, and T. Neupert, Higher-order topological insulators, *Sci. Adv.* **4**, 6 (2018).
 - [32] B. Y. Xie, H. F. Wang, H. X. Wang, X. Y. Zhu, J. H. Jiang, M. H. Lu, and Y. F. Chen, Second-order photonic topological insulator with corner states, *Phys. Rev. B* **98**, 205147 (2018).
 - [33] I. Petrides, and O. Zilberberg, Higher-order topological insulators, topological pumps and the quantum Hall effect in high dimensions, *Phys. Rev. Res.* **2**, 22049 (2020).
 - [34] W. A. Benalcazar, J. Noh, M. Wang, S. Huang, K. P.

- Chen, and M. C. Rechtsman, Higher-order topological pumping, arXiv:2006.13242.
- [35] R. Seshadri, A. Dutta, and D. Sen, Generating a second-order topological insulator with multiple corner states by periodic driving, *Phys. Rev. B* **100**, 115403 (2019).
 - [36] M. Ezawa, Higher-Order Topological Insulators and Semimetals on the Breathing Kagome and Pyrochlore Lattices, *Phys. Rev. Lett.* **120**, 026801 (2018).
 - [37] M. Ezawa, Minimal models for wannier-type higher-order topological insulators and phosphorene, *Phys. Rev. B* **98**, 045125 (2018).
 - [38] M. Ezawa, Strong and weak second-order topological insulators with hexagonal symmetry and \mathbb{Z}_3 index, *Phys. Rev. B* **97**, 241402(R) (2018).
 - [39] L. Trifunovic and P. W. Brouwer, Higher-Order Bulk-Boundary Correspondence for Topological Crystalline Phases, *Phys. Rev. X* **9**, 011012 (2019).
 - [40] Z. Yan, F. Song, and Z. Wang, Majorana Corner Modes in a High-Temperature Platform, *Phys. Rev. Lett.* **121**, 096803 (2018).
 - [41] Q. Wang, C.-C. Liu, Y.-M. Lu, and F. Zhang, High-Temperature Majorana Corner States, *Phys. Rev. Lett.* **121**, 186801 (2018).
 - [42] R. Chen, C.-Z. Chen, J.-H. Gao, B. Zhou, and D.-H. Xu, Higher-order Topological Insulators in Quasicrystals, *Phys. Rev. Lett.* **124**, 036803 (2020).
 - [43] M. Serra-Garcia, V. Peri, R. Süssstrunk, O. R. Bilal, T. Larsen, L. G. Villanueva, and S. D. Huber, Observation of a phononic quadrupole topological insulator, *Nature (London)* **555**, 342 (2018).
 - [44] C. W. Peterson, W. A. Benalcazar, T. L. Hughes, and G. Bahl, A quantized microwave quadrupole insulator with topologically protected corner states, *Nature (London)* **555**, 346 (2018).
 - [45] Z. X. Su, Y. Z. Kang, B. F. Zhang, Z. Q. Zhang, and H. Jiang, Disorder induced phase transition in magnetic higher-order topological insulator: A machine learning study, *Chin. Phys. B* **28**, 117301 (2019).
 - [46] Z. Q. Zhang, B. L. Wu, C. Z. Chen, and H. Jiang, Global Phase Diagram of disordered Higher-order Weyl Semimetals, *Phys. Rev. B* **104**, 014203 (2021).
 - [47] C. Wang, X. R. Wang, Robustness of Helical Hinge States of Weak Second-Order Topological Insulators, *Phys. Rev. B* **103**, 115118 (2021).
 - [48] C. Wang, X. R. Wang, Disorder-Induced Quantum Phase Transitions in Three-Dimensional Second-Order Topological Insulators, *Phys. Rev. Research* **2**, 033521 (2020).
 - [49] H. Liu, J.-K. Zhou, B. L. Wu, Z.-Q. Zhang, and H. Jiang, Real space topological invariant and higher-order topological Anderson insulator in two-dimensional non-Hermitian systems, *Phys. Rev. B* **103**, 224203 (2021).
 - [50] Y.-S. Hu, Y.-R. Ding, J. Zhang, Z.-Q. Zhang, and C.-Z. Chen, Disorder and phase diagrams of higher-order topological insulators, *Phys. Rev. B* **104**, 094201 (2021).
 - [51] M. Ezawa, Topological switch between second-order topological insulators and topological crystalline insulators, *Phys. Rev. Lett.* **121**, 116801 (2018).
 - [52] C. Chen, Z. Song, J. Z. Zhao, Z. Chen, Z. M. Yu, X. L. Sheng, and S. A. Yang, Universal Approach to Magnetic Second-Order Topological Insulator, *Phys. Rev. Lett.* **125**, 56402 (2020).
 - [53] W. A. Benalcazar, J. Noh, M. Wang, S. Huang, K. P. Chen, M. C. Rechtsman, Higher-order topological pumping and its observation in photonic lattices, *Phys. Rev. B* **105**, 195129 (2022).
 - [54] I. Petrides and O. Zilberberg, Higher-order topological insulators, topological pumps and the quantum Hall effect in high dimensions, *Phys. Rev. Research* **2**, 022049R (2020).
 - [55] Y. Tanaka, R. Takahashi, R. Okugawa, and S. Murakami, Roto-inversion-symmetric bulk-hinge correspondence and its applications to higher-order Weyl semimetals, *Phys. Rev. B* **105**, 115119 (2022).
 - [56] S. Datta, *Electronic transport in mesoscopic systems*, Cambridge, 1995.
 - [57] A. M. Guo, and Q. F. Sun, Topological states and quantized current in helical organic molecules, *Phys. Rev. B* **95**, 155411 (2017).
 - [58] Z. Q. Zhang, C. Z. Chen, Y. J. Wu, H. Jiang, J. W. Liu, Q. F. Sun, X. C. Xie, Chiral Interface States and Related Quantized Transport in Disordered Chern Insulators, *Phys. Rev. B* **103**, 075434 (2021).